Journal Pre-proofs

Carbon-modified titanium oxide materials for photocatalytic water and air de-contamination

Mariana R.F. Silva, Mirtha A.O. Lourenço, David Maria Tobaldi, Carla F. da Silva, Maria Paula Seabra, Paula Ferreira

Please cite this article as: M.R.F. Silva, M.A.O. Lourenço, D.M. Tobaldi, C.F. da Silva, M.P. Seabra, P. Ferreira, Carbon-modified titanium oxide materials for photocatalytic water and air decontamination, *Chemical Engineering Journal* (2020), doi: https://doi.org/10.1016/j.cej.2020.124099

This is a PDF file of an article that has undergone enhancements after acceptance, such as the addition of a cover page and metadata, and formatting for readability, but it is not yet the definitive version of record. This version will undergo additional copyediting, typesetting and review before it is published in its final form, but we are providing this version to give early visibility of the article. Please note that, during the production process, errors may be discovered which could affect the content, and all legal disclaimers that apply to the journal pertain.

Carbon-modified titanium oxide materials for photocatalytic water and air decontamination

Mariana R. F. Silva,[1] Mirtha A. O. Lourenço,[*1,2] David Maria Tobaldi,[1] Carla F. da Silva,[1] Maria Paula Seabra[1] and Paula Ferreira[*1]

[1]CICECO – Aveiro Institute of Materials, Department of Materials & Ceramic Engineering, University of Aveiro, 3810-193 Aveiro, Portugal

[2]present address: Istituto Italiano di Tecnologia, Center for Sustainable Future Technologies, Via Livorno, 60, 10144 Torino TO, Italy

*Corresponding authors: mirtha@ua.pt; pcferreira@ua.pt, +351 234401419, Fax: +351 234401470

KEYWORDS

ABSTRACT

Titanium oxide-based materials with different physical and chemical features were synthetized aiming at removing organic pollutants from both water and air media. The materials were produced employing two different heating methodologies (thermal, T and hydrothermal, H) at distinct temperatures resulting in porous materials. These materials were also modified with either graphene oxide (GO) or carbon nanotubes (CNT), using an in-situ approach. All materials were tested as photocatalysts using ultra-violet (UV), visible (Vis) and solar radiation. Rhodamine B (RhB) and benzene were used as representative pollutants in water and air, respectively.

The addition of carbon to the catalysts improved the removal of both pollutants. In the case of the photocatalytic degradation of rhodamine B, under both UV and Vis light, it was found that, the materials containing carbon nanostructures allowed the highest degradation degree, while the photosensitisation phenomenon became negligible. The best catalyst is the one containing CNT (2.98 wt.% of C) and thermally treated at 300 °C (**T300_CNT**). This material showed higher degradation ability than the commercial TiO_2 nanopowder Degussa P25 (**P25**) under Vis light. Regarding benzene removal, the samples thermally

treated at 300 °C and modified with CNT and GO (**T300_CNT** and **T300_GO**, respectively) outperformed Degussa P25. The former material was successfully reused in the photocatalytic degradation of benzene over 6 consecutive cycles.

1. INTRODUCTION

Environmental pollution, water and air pollution, is a wide-spreading issue impacting not only human life but also all living beings [1–3]. Regarding water pollution, it has been estimated that over 800,000 tons of synthetic dyes are produced annually worldwide [4], approximately 10-15% of which are discharged without proper treatment, through industrial effluents, draining in natural watercourses [5]. The release of synthetic dyes to the aquatic medium is coming from numerous industries. The biggest contributor in this issue is the textile industry [6,7], followed by, in no particular order, the leather tanning [8], paper [9], hair-colouring [10] and food industries [11]. This is of concern due to dyes bioaccumulation in both fauna and flora [12]. For instance, the presence of small amounts of azo dyes (the most used type of dye) in water can decrease sun-light penetration diminishing photosynthetic activity, which results in lower biota growth as well a minor dissolved oxygen concentration. This has an acute toxic effect on both the aquatic flora and fauna, disturbing ecosystem's balance [13–15]. Additionally, some dyes may even cause allergies, skin irritation and cancer to humans [13,16,17]. Their partial degradation can also be equality worrisome since the by-products might be more toxic than the original dyes [12]. Thus, it is urgent to remove organic dyes from water and to promote the proper wastewater treatment of the contaminated waters. In order to mitigate this issue, several methodologies are currently being studied and employed for the degradation and/or removal of these dyes: ozonation [18–20], electrochemical oxidation [21], bacterial and/or fungal degradation [22,23], biosorption [24], phytoremediation [25] and photocatalysis [26–28]. From those, photocatalysis has the advantage to allow for complete mineralisation of the dyes, using low-cost catalyst system and relatively simple setups. It is also a faster method than, for instance, biological treatments which have very slow reaction rates and requires a tight control of the process conditions (microbial growth conditions) [29].

In the case of air pollution, the emission of volatile organic compounds (VOC), coming from anthropogenic sources, has also a significant negative impacts in human [30–34] and

environmental health [35,36]. Benzene is an well-known VOC and has been classified as a Group I (carcinogenic to humans) by the International Agency for Research on Cancer (IARC) [37]. Consequently, significant efforts have been made in the removal of VOC, and namely benzene. It should be noticed that high-concentrated VOC emitted from industrial plants can be removed by adsorption [38], catalytic combustion [39,40] or biological methods [41,42]. However, in the case of VOC in low concentrations, due to their limited interaction with active species, they are hardly degraded by a single method [43]. Thus, the current conventional approach eliminates these lower concentrated VOC by, first concentrating them followed by a catalytic combustion. The latter is a high energy demanding process and cannot be used in multiple environmental conditions such as indoor. Thus, it is extremely desirable to develop efficient processes towards complete oxidation of low-concentrated VOC that work in mild conditions and are energy-saving and safe [43]. Photocatalysis is a feasible methodology, since even low concentrations of VOC can be degraded [44,45].

Photocatalysis is a process initiated by light that, with the help of a catalyst, can degrade dyes and VOC. TiO_2, due to its biological and chemical inertness, high activity, low cost, non-toxicity along with durability regarding photo and chemical corrosion, is the photocatalyst most frequently used [46–48]. However, the band gaps of TiO_2 polymorphs (3.2 eV, 3.02 eV and 3.1-3.4 eV for anatase, rutile and brookite, respectively [49,50]) show that these materials are activated only with UV light. Additionally, the wide band-gap energy of TiO_2 may induce fast recombination of electron-hole pairs, which may extensively restrict the photoconversion efficiency [51]. Consequently, it is paramount to find photocatalytic materials that can be activated with Vis light and that have a better performance using solar light (5% UV (300–400 nm), 43% Vis (400–700 nm), and 52% infrared (700–2500 nm) [52]), that is free and available [49]. Therefore, strategies have to be developed in order to reduce the energy required to eject the electron from the valence band (VB) to the conduction band (CB), creating the electron-hole pairs that will then generate free radicals which would be involved in the secondary reaction capable of degrading pollutants such as dyes [50]. Moreover, it is also necessary to reduce the amount of electron-hole recombination. The most used strategy involves modifying the TiO_2 with metals [53,54], carbon structures (carbon nanotubes [55,56], graphene oxide [57,58],

reduced graphene oxide [55,59]) or other assorted dopants (metal oxides, nitrogen, etc.) [60–63]. Besides photocatalysis, photosensitization (the photon is absorbed by the dye) can also occur [64]. The charge is then transferred from the excited dye molecule to the semiconductor CB resulting in the formation of an unstable dye cation radical and, in parallel, an active species on the semiconductor surface that attacks the destabilized dye molecule. However, this process results in the incomplete degradation of the dye and is much slower ($\approx$ 2 or 3 orders of magnitude) than the photocatalytic one [65], the latter being the most desirable one.

Tremendous progress can be expected in the environment if one is able to design a sustainable, versatile, cost efficient and effective photocatalyst that removes critical organic pollutants from both aquatic and air media. This work presents, for the first time, a complete study on carbon modified TiO_2-based porous particles, comprising the materials physical and chemical characterization and also their functionality by means of water and air purification. Macro- and meso-porous TiO_2-based materials employing different processing treatments (thermal and hydrothermal) and temperatures (60, 180, 300 and 500 °C) were synthesized through a very simple and low energy wasting method. To enhance the photocatalytic activity under both UV and Vis light, graphene oxide and carbon nanotubes TiO_2 composites were prepared and investigated. These easy to make materials were tested, for the first time, in the photodegradation of RhB, as organic dye pollutant model, under UV and Vis lights and their photocatalytic behaviour was evaluated and compared with the commercial TiO_2 material, Degussa P25. The versatility of the synthesized materials was also examined by testing the most promising samples in the gaseous removal of benzene, used as a model of a VOC, under solar light. Their ability to be reused as an air purification catalyst was determined by exposing the materials to several cycles of polluted air.

2. EXPERIMENTAL DETAILS

2.1. *Chemicals and Reagents*
Tetrabutyl orthotitanate (TBOT, 97% Fluka), P25 TiO_2 nanoparticles (~20 nm diameter, Degussa), CNT, multi-walled carboxylic acid functionalized (>8% carboxylic acid

functionalized, avg. diam. × L is 9.5 nm × 1.5 μm, Aldrich), rhodamine B (Sigma), benzene 4.87 mol.PPM^{-1} (Praxair) and pure synthetic air (Praxair) were used as received.

The GO was prepared through the Hummers method [66], using graphite flakes, phosphoric acid (99%), sulphuric acid (95-98%), potassium permanganate (99%), hydrogen peroxide (30%), hydrochloric acid (36.5-38.0%) and diethyl ether (99%), all from Sigma-Aldrich.

2.2. *Titanium oxide-based materials synthesis*

Three different methodologies (i, ii and iii) were followed resulting from significant modification of a procedure described in the literature [47]. Thus, it was employed a two-step procedure, starting by hydrolysis and condensation of the TBOT precursor followed by thermal treatment at different conditions. The procedures are as follows:

   i) Pure TiO$_2$ materials were made by dropping TBOT onto distilled water at room temperature (1:10 w/w), with no stirring.

   ii) TiO$_2$ materials containing GO were obtained by first mixing the GO (5 wt% of TBOT) and the distilled water through 10 min of stirring, followed by dropwise addition of TBOT to this mixture (1:10 w/w) without stirring.

   iii) TiO$_2$ with CNT materials were prepared by adding CNT (1 wt% of TBOT) to TBOT and sonicating (42 kHz) for 30 min. The CNT-TBOT mixture was added dropwise onto distilled water (1:10 w/w), with no stirring.

Then two treatments were tested: thermal (T) or hydrothermal (H). The thermal treatment was made by leaving the materials to age for 24 h; after the precipitates were removed, rinsed with distilled water repeatedly (5 times), and then left to dry in a Petri dish at ambient conditions for 24 h. The resulting materials were thermally treated at: 60, 300 and 500 °C. Regarding the materials subjected to the hydrothermal treatment, after obtaining the mixture (some with GO or CNT), they were putted into an autoclave and left in an oven for 24 h at 180 °C. Then, the powders were washed repeatedly (5 times) with distilled water and dried at 60 °C overnight.

The samples are named with the code: *xy_z*. The *x* corresponds to the type of treatment employed: **T** for thermal and **H** for hydrothermal (using Teflon-lined autoclaves under autogenous pressure); *y* corresponds to the temperature used (T samples 60, 300 or 500 °C, and in H samples 180 °C). Lastly, *z,* when present in the samples designation, stands for the

presence of graphene oxide (GO) or carbon nanotubes (CNT). For example, the sample made by thermal treatment at 500 °C and with addition of GO is denominated T500_GO. For comparison reasons, GO and CNT were also calcinated at 300 ºC.

2.3. *Materials characterization*

The materials prepared in this study were characterized by powder X-ray diffraction (XRD), scanning electronic microscopy (SEM), scanning-transmission electronic microscopy (STEM), low temperature (-196 ºC) nitrogen adsorption-desorption isotherms, RAMAN, ATR-FTIR and differential reflectance (DRS) spectroscopies, thermogravimetric analysis (TGA), elemental analysis (EA). For the functional properties of the materials, photocatalytic degradation tests with RhB and benzene were carried out. In addition to this, scavenging tests with RhB and the quenchers ethylene-diamine-tetra-acetic acid (EDTA), p-benzoquinone (BQ), and isopropyl alcohol (IPA) were performed. Equipment and experimental parameters used are described in the Electronic Supplementary Information (ESI).

2.4. *Photocatalytic tests (liquid-solid phase)*

The photocatalytic efficiencies of TiO_2-based catalysts were measured in the liquid– solid phase, by monitoring the degradation of RhB, using a spectrometer (Shimadzu UV 3100, JP). Tests were performed at room temperature, in a cylindrical photocatalytic reactor (80 mm in diameter) containing an aqueous solution of the dye (0.2 L), at an initial concentration of 5 mg/L. The concentration of the photocatalyst in the slurry was 0.125 g/L. To mix the solution thoroughly, the slurry was magnetically stirred throughout the reaction; the reactor was covered with a watch-glass, so as to avoid the evaporation of the solution. The lighting of the reacting system was achieved by placing a lamp at the top of the reactor. The UV-A and Vis light, with an irradiance of approximately 3.25 and 80 W/m^2, respectively – measured with a radiometer (Delta OHM, HD2302.0, IT).

The photocatalytic degradation of RhB was controlled by sampling 6 mL of the slurry, at regular time intervals. Before switching on the light to initiate the photocatalytic reaction, the suspension was stirred in the dark for 30 min, so that adsorption/desorption of the material(s) regarding RhB could be assessed. The RhB concentration was ascertained using

the Lambert–Beer law. To apply this law, the absorbance of RhB was measured at 554 nm using a spectrometer using distilled water as reference. Before the analysis, the photocatalytic particles were separated and removed from the RhB solution through centrifugation. Additionally, to understand the role of active radical species in the photocatalytic (PC) process and gain insight into the PC reaction mechanism, experiments using scavengers were also assessed.[67] At this purpose, 2×10^{-4}mol (in 200 mL of solution) of ethylene-diamine-tetra-acetic acid (EDTA), p-benzoquinone (BQ), and isopropyl alcohol (IPA) were added to the reacting system to selectively scavenge holes (h^+), superoxide radicals ($\cdot O^{2-}$) and hydroxyl radicals ($\cdot OH$), respectively. The tests used RhB (initial concentration of 5 mg/L) and visible light (36.5 W/m^2) as the radiation source.

2.5. *Photocatalytic tests (gas-solid phase)*

The PC efficiency in the degradation of benzene was tested. The reactor employed for the gas−solid phase tests operates in continuous conditions, as previously described in detail by Tobaldi *et al.* [68]. The reactor was made of a stainless-steel cylinder (3.8 L in volume). Its top was sealed and covered with a glass window, to allow the light to reach the photocatalyst placed inside it. The light source employed was a solar lamp (Osram Ultra-Vitalux, 300 W) placed at 20 cm from the photocatalyst reaching a radiance intensity of 39.6 W/m^2 in the UV-A region and 278.0 W/m^2 in the visible. The tests were carried out at 25±1 °C (temperature inside the reactor) with a relative humidity of 37%, measured via a thermocouple that was placed inside the chamber, and a humidity sensor placed in the inlet pipe. The aforementioned parameters were controlled and found to remain stable throughout the experiment. The concentration of the pollutant gas was measured in the outlet of the chamber by a VOC-72M gas analyser (Environment SA, FR), which quantifies its concentration based on gas chromatography and photo-ionisation detection.

Before starting the experiment, a petri dish with 0.1 g of the PC material in powder form is placed inside the reactor. Initially, the glass window in the reactor is covered so that the sample is kept in the dark until the gas concentration in the chamber is stable at the desired level of about 250 μg/m^3 (~77 ppb). This concentration was chosen following the World Health Organisation recommendation of an exposure to total VOCs < 300 μg/m^3 in average during 8 h/day [69]. Once the required conditions were met, the window glass was

uncovered, the lamp turned on, and the PC reaction started. The inlet gas used was a mixture of prepared gas cylinders of synthetic air and the chosen pollutant, C_6H_6.

The mixed air was continuously monitored, and the total flow rate kept constant at 150 mL/min by two flow controllers, one for the synthetic air and the second for the pollutant. During the test, continuous flow in the reactor was necessary to ensure the sample saturation, guarantying that only the PC process was involved (i.e., no absorption from the sample nor from the reactor walls) [70].

Commercial TiO_2 Degussa P25 (P25) was used as reference in all of the PC activity tests.

3. RESULTS AND DISCUSSION

3.1. Characterization of materials

The physical and textural properties of the TiO_2-based materials are studied by XRD, -196 °C N_2 adsorption/desorption isotherms and SEM. Figure 1 shows the XRD patterns of all TiO_2-based materials prepared in this work.
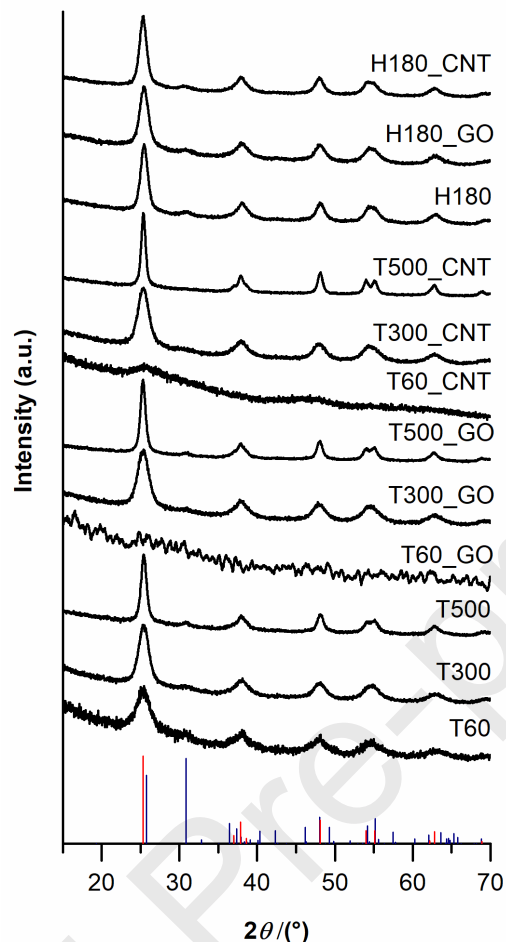
Figure 1. XRD patterns of TiO_2-based materials. The blue bars refer to brookite JCPDF reference card (04-007-6488) and those in red to anatase JCPDF reference card (04-016-2837).

The T60 material is constituted by poorly crystalline anatase and brookite TiO_2 polymorphs; whereas T60_GO and T60_CNT are mainly amorphous. This difference is probably due to addition of the carbon-based materials, GO and CNT, to the titanium precursor (TBOT) which partially blocks the mobilisation of the polymeric Ti-O-Ti chains leading to an increase to the necessary energy to the crystallisation process [71,72]. All the other samples, with the exception of T500_CNT, are composed of both brookite and anatase, while T500_CNT only has anatase.

Figure S1 and Table 1 present the data obtained by -196 °C N_2-sorption isotherm of the TiO_2-based materials. The sample T60 displays a mixture of types Ib and IV isotherms, although when GO or CNT are added, the isotherms are Type Ib (IUPAC classification

[73]). All other materials (the non- and carbon-modified TiO_2 treated at 180, 300 and 500 °C) are Type IV. Type Ib isotherms are typical in materials with wide-range pore size distributions from broader micropores and perhaps narrow mesopores ($<\sim$2.5 nm). Type IV isotherms are typically detected on conventional mesoporous materials having adsorbent-adsorptive interactions [73].

Table 1. Physical properties of the produced materials.

Treatment	Thermal (T)									Hydrothermal (H)		
Added	**-**			**GO**			**CNT**			**-**	**GO**	**CNT**
Temperature	60	300	500	60	300	500	60	300	500	180	180	180
S_{BET} (m^2/g)	335	199	101	459	172	68	440	205	65	152	186	164
V_P (cm^3/g)	0.20	0.29	0.21	0.13	0.19	0.08	0.16	0.24	0.11	0.31	0.24	0.31
d_P (nm)[a]	2.7	5.5	7.9	1.9	4.2	5.7	2.3	3.3	5.6	8.0	5.6	8.0

[a]Pore width obtained from the BJH method with the corrected Kelvin equation, i.e. KJS–BJH method at the maximum of pore size distribution calculated based on adsorption data.

The specific surface areas (S_{BET}) of thermal treated materials (T) at 60 °C are the highest, increasing with the presence of carbon nanostructures (459 and 440 m^2/g in the case of T60_GO and T60_CNT, respectively, versus 335 m^2/g in T60). For higher temperatures, the opposite is observed, the S_{BET} decreases with the increase of the temperature of treatment to 300 and 500 °C. This observation is probably due to the densification of the material with temperature along with collapse of smaller pores decreasing surface area [74,75]. This idea is supported by the increase of pore width (d_P) with the increase in temperature. It should be remarked that all materials treated at 300 °C have S_{BET} around 200 m^2/g.

Regarding the S_{BET} of hydrothermally treated material containing GO (H180_GO) has the highest S_{BET} (186 m^2/g) followed by H180_CNT (164 m^2/g) and lastly H180 (152 m^2/g). The addition of carbon materials appears to increase the S_{BET}, in the H samples, but no trend is observed in the case of the pore volume (V_P) and pore width (d_P).

The SEM micrographs (Figures 2 and S2, ESI) confirm the presence of pores (corroborated by the low angle reflection in the XRD pattern of Figure S3, ESI) in multiples materials but more distinctly in samples T60 and T60_GO (macropores). Figure S2 shows that, in

general, with the increase of temperature and pressure the materials seem to become dense. The T300_GO (Figure 2E) appears to have a film covering the titanium dioxide which is probably graphene oxide. The materials with carbon nanotubes (Figure 2 C and F) seem less compact, which corroborates the higher S_{BET} (Table 1) observed in this family of materials, when compared with the homologous ones. However, the presence of pores is not detected via SEM.
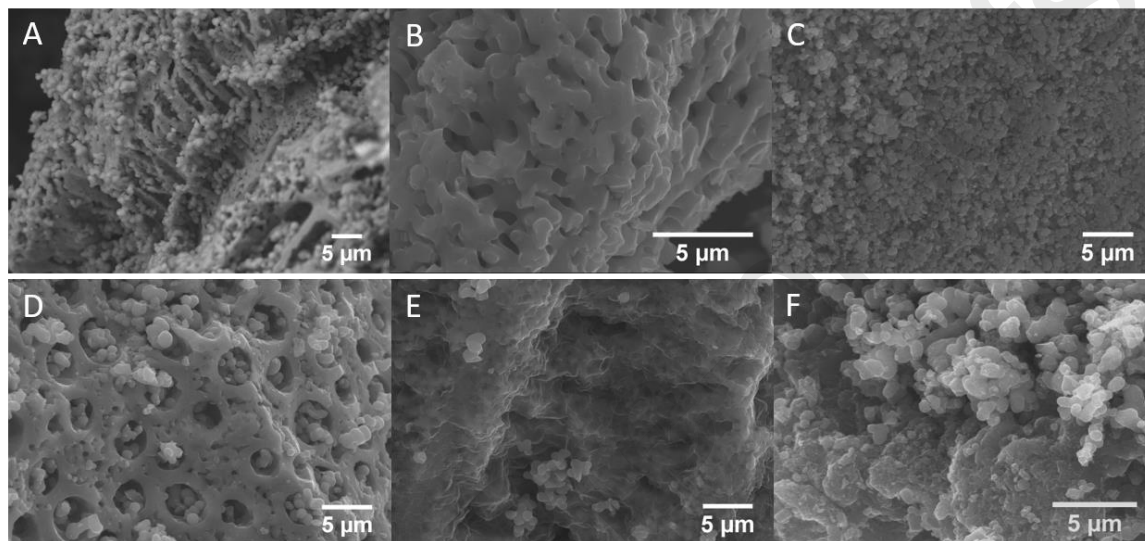

Figure 2. SEM micrographs of: A) T60; B) T60_GO; C) T60_CNT; D) T300; E) T300_GO; and F) T300_CNT.

STEM analyses were carried out in samples T300, T300_GO and T300_CNT (Figure 3) to confirm the microstructure and the way as GO and CNT was incorporated on the TiO_2 materials (in T300_GO and T300_CNT, respectively). Figure 3A and 3B show the absence of any carbon-based material in T300. In Figures 3C and 3D, it is possible to verify the presence of a layer of GO around the TiO_2 particles in the T300_GO material. Figure 3E and 3F, the carbon nanotubes are visible, confirming their presence in T300_CNT material. Ultra-high resolution TEM (UHRTEM) was performed (Figure S4, ESI) on samples T300, T300_GO and T300_CNT. In T300 the particles d-spacing measurement (0.363 nm) correspond to (101) plane of tetragonal anatase crystal structure, which align with the XRD results (Figure 1) [76]. In T300_GO, TiO_2 particles are visible along with some GO surrounding then, as already observed at the STEM (Figure 3C and 3D). In the T300_CNT

sample, TiO_2 particles as well as carbon nanotubes (multiwalled carbon nanotubes-MWCNTS) can be observed.
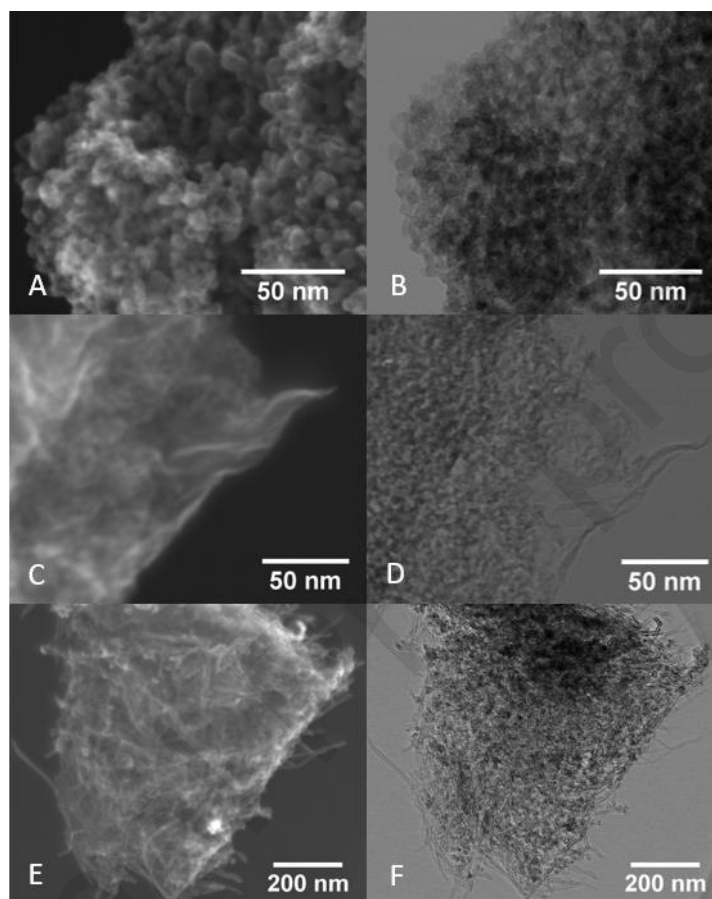

Figure 3. STEM images of: A) T300 SEM mode; B) T300 TEM mode; C) T300_GO SEM mode; D) T300_GO TEM mode; E) T300_CNT SEM mode; and F) T300_CNT TEM mode.

Elemental analysis also confirmed that carbon remains in the materials after thermal treatment at 300 °C. For instance, the sample containing CNT has approx. 3.1% of carbon while the sample with GO contains residual carbon amounts (Table S1).

Raman analysis, presented in Figure S5 (ESI), is made to confirm the polymorph(s) present in the samples along with the incorporation of carbon-based materials (GO and CNT). The typical reference bands for anatase are: a very strong band at 144 cm^{-1}, medium intensity

bands at 399, 507, 519, 640 cm^{-1}, and weak bands at 197 and 796 cm^{-1}[77]. Brookite has characteristic strong bands at 128 and 636 cm^{-1}, a very strong band at 153 cm^{-1} and a medium strength one at 247 cm^{-1} [78]. It also has numerous weak bands – 135, 195, 214, 288, 322, 366, 412, 454, 461, 502, 545 and 585 cm^{-1} [78]. Thus, unmodified TiO$_2$ samples show, for all thermal treatment conditions, bands assigned to anatase and brookite. The bands associated with brookite TiO$_2$ polymorph are mainly observed for T60 (at 153 cm^{-1}) and in H180 at 249, 277, 320 and 364 cm^{-1}. In T300 the brookite bands are at 244, 279, 319 and 364 cm^{-1} and in T500 appears at 245, 275 and 322 cm^{-1}. The anatase bands exist in all aforementioned samples with very strong bands at around 144 cm^{-1} and medium intensity ones about 515 and 640 cm^{-1}. These results are in agreement with those obtained by XRD (Figure 1). In the case of the TiO$_2$ samples with GO, the bands of brookite are not observed by Raman spectroscopy. This lack of visibility of brookite bands is due to its overlapping by the presence of the GO bands (D band at 1357 cm^{-1}, G band at 1600 cm^{-1} [79] and 2D or G' band 2670 cm^{-1} [80]). Only in sample T500_GO, where the high temperature leads to GO degradation, can the brookite peaks be observed at – 193, 244, 272, 321, 362 and 434 cm^{-1}. Regarding samples with CNT, as in GO ones, the addition of the CNT (1356 cm^{-1} D-band; 1591cm^{-1} G-band; 1754 and 1775 cm^{-1} M-bands; and 2704 cm^{-1} G' band [81]) prevents the brookite peaks from being seen. In sample T500_CNT the CNT are degraded [82] (supported by TGA Figure S6, ESI), so the Raman only shows peaks regarding the TiO$_2$, particularly just for anatase, which confirms the XRD results (Figure 1). Figure S7a shows the comparison of the Raman spectra of the samples GO, GO calcinated at 300 ºC and T300_GO. The D and G bands in the GO samples are poorly observed. After calcination of GO at 300 ºC it is possible to observe an increase of the intensity of the D and G bands located at 1310 cm^{-1} and 1599 cm^{-1}. This phenomenon is compatible with the reduction of GO with temperature as observed by Sengupta *et al.*.[83] Besides the anatase and brookite bands, T300_GO sample also presents the two typical features of GO, the D and G bands located at 1311 cm^{-1} and 1601 cm^{-1} respectively. Thus, the *in-situ* modification of TiO$_2$ with GO followed by calcination at 300 ºC promotes a small red-shift on D band and a blue-shift on the G band regarding the GO_300 sample, suggesting GO surface strain after combination with TiO$_2$ *via* C–O–Ti bonds formation.[84] Figure S7b on the other hand display the Raman spectra of the samples CNT, CNT_300 (calcinated at 300 ºC) and

T300_CNT. The calcination of the CNT at 300 °C leads to the increase of the G band, suggesting an increase of the sp^2 carbon systems and consequently the presence of more graphitic species. In the CNT_300 sample, D and G bands are located at 1291 cm^{-1} and 1601 cm^{-1}. In the case of the T300_CNT, just an up-shift of the D (1312 cm^{-1}) band is observed, when comparing with the CNT_300 sample, that can be associated to stress produced by the TiO_2 linked to the surface of the CNT.[85,86]

The comparison of the ATR-FTIR spectra of GO, CNT and carbon modified TiO_2 samples calcinated at 300 °C are showed in Figure S8. The T300 sample presents a broad absorption peak around 500 cm^{-1}, that can be assigned to the Ti–O–Ti stretchings vibrations. Additionally, an absorption peak around 3346 cm^{-1} is observed related to the presence of the O–H stretching vibrations associated to the surface hydroxyl groups.[84] In the case of GO, it is possible to observe that the increase of temperature at 300 °C leads to the elimination of oxygen-containing functional groups. The GO sample has a broad peak around 3360 cm^{-1} associated to the presence of –OH group that almost disappears after calcination of GO at 300 °C. This is in agreement with the reduction of GO. Moreover, GO also shows typical peaks at 1729, 1402 (broad), and 1032 cm^{-1} assigned to the carboxylate C=O stretching, carboxyl C–O, epoxide C–O–C or phenolic C–O–H, and alkoxy C–O, respectively, that after the thermal treatment are highly reduced.[83] The peak at 1623 cm^{-1} is assigned to C=C bond, that became part of the skeletal vibration of reduced GO sheets. [87] In the case of CNT samples (CNT and CNT_300), the IR spectra shows a small peak around 1670 cm^{-1} that can be assigned to the C=C stretching bands [88]. The modification of TiO_2 with GO and CNT leads with a slight shift in the broad band at 500 cm^{-1} suggesting the presence of Ti–O–C bonds in both materials. Additionally, slight GO and CNT bands are observed in T300_GO and T300_CNT between the range 1000 – 1700 cm^{-1} when comparing with the pristine carbon materials [89,90]. Moreover, both T300_GO and T300_CNT have two additional peaks around 2895 and 2992 cm^{-1} associated to the presence of the sp^3 and sp^2 carbon stretching vibrations, respectively [91].

XPS analyses (Figure S9, ESI) was used to further confirm the interactions between TiO_2 and GO. An overview of the XPS spectra of the samples T300, T300_GO and T300_CNT is shown in Figure S9a. The survey VIAspectrum shows the presence of the Ti, O and C element in all materials indicating that the TiO_2-carbon based materials were successfully

prepared. In the Ti2p spectrum of T300 (Figure S9b) the binding energies of $Ti2p_{1/2}$ and $Ti2p_{3/2}$ are observed at 464.4 and 458.7 eV, respectively, which are assigned to the binding energy of Ti^{4+} in TiO_2.[84,92] The shoulder $Ti2p_{1/2}$ at 460.0 eV corresponds to Ti^{3+} chemical state of in Ti_2O_3 [93]. The addition of GO and CNT to the TiO_2 in both T300_GO and T300_CNT materials does not significantly change the Ti2p spectrum, and no band related to the Ti–C bond is observed [94] as it was expected from the other analyses. The O1s spectra is presented in Figure S9c. The T300 material shows peaks centred at 529.7 (74.8%), 530.5 (17.2%), 531.1 (6.1%) and 535.6 eV (1.9%) assigned to Ti–O–Ti (lattice O), Ti–O–C, Ti–OH and C–OH groups, respectively.[95] The existence of the Ti–O–C bond in this sample can be related to some remaining carbon from the precursor or adsorption of CO_2 from air at the surface, and the Ti–OH species observed are assigned to the hydroxyl groups at the surface of the TiO_2. The successful modification of TiO_2 with carbon in the samples T300_GO and T300_CNT can be observed by the increase of the amount of Ti–O–C species to 55.7% and 18.5%, respectively. The percentages for the Ti–O–Ti, Ti–OH and C–O are 16.0, 25.9 and 2.4 eV in the T300_GO material and 72.8, 6.7 and 2.0 eV in the T300_CNT material, respectively, indicating that the modification of TiO_2 with CNT disturbed the structure of the TiO_2 less than the GO, maintaining the amount of the Ti–O–Ti species and reducing significantly the amount of the Ti–OH species. The C1s spectra of these samples are presented in Figure S9d. All materials possess bands located at binding energies of 284.7 and 285.5 eV that can be assigned to sp^2 and sp^3 carbons species, respectively [94]. The amount of sp^3 species in the sample T300 is higher than 52% demonstrating that the carbon present in this sample is mostly amorphous. The successfully incorporation of GO and CNT materials can be observed by the increase of the amount of sp^2 species in the C1s spectrum. The bands observed at *ca.* 287.0 and at 289.2 eV are assigned to C–O, C–OH and C=O groups in all materials, respectively.[94] The band at 291.9 eV corresponds to the π-π* transitions.

Figure S6 (ESI), shows the TGA of T60, T60_GO and T60_CNT materials up to 800 °C. The weight loss observed below 100 °C is related to desorption of physiosorbed water for all samples. At 300 °C, T60 sample shows an almost complete degradation of some remaining carbon content from the TBOT precursor and a weight loss of about 18.6% up to this temperature. After this temperature and up to 800 °C this sample losses are negligible,

ca. 1.2% of weight that can be associated to the release of oxygenated species during the crystallization of TiO_2 [96]. When compared with T60, both T60_GO and T60_CNT present a wide-large peak at around 80 ℃, that corresponds to water desorption, degradation of organic contents (from the titanium precursor) and partial degradation of GO or CNT. From room temperature up to 300 °C, T60_GO and T60_CNT have a weight loss of 22.3% and 23.4%, respectively. The degradation of GO below 300 ℃ under air involves the removal of oxygenated groups (hydroxyl, epoxy, and carboxyl groups) and the formation of defects on the graphene basal planes (by removing some carbon atoms) which is agreement with Pan *et al.* and Pastrana-Martínez [97,98]. The slow weight loss between 300 – 500 °C can be related to the elimination of more stable oxygen functionalities, while the slow weight loss after 500 °C corresponds to carbon combustion of the remained GO [98,99]. Mahajan *et al.* [82] studied the TG curve of CNTs (multiwalled CNT) conducted in air and observed that MWCNT are thermally stable up to 420 °C. Above this temperature, weight loss starts to occur due to the oxidation of the remaining amorphous carbon and of MWCNTs themselves. This result agrees with those observed in this present study. Actually, the last weight loss (*ca.* 4%) of T60_CNT sample starts at about 450 °C, meaning that at 500 °C (the temperature of the thermal treatment) low amounts of CNT are present in the sample, and they should be deformed (MWCNT deterioration and bundles formation) as observed by Mahajan *et al.* [82].

Band-gap values (Table 2) can give a general idea of the amount of energy needed to provide to the catalyst in order for an electron to move from the valence band to the conduction band and ideally start the photocatalytic process. The band gap values presented in Table 2 are calculated by employing the Tauc plot method [100]. An optical spectrum of reflectance *vs* wavelength is displayed in Figure S10 (ESI).

Table 2. Band-gap values of samples T*y*(_*z*) and H*y*(_*z*).

Treatments	Thermal (T)									Hydrothermal (H)		
Filler	**-**			**GO**			**CNT**			**-**	**GO**	**CNT**
Temperature	60	300	500	60	300	500	60	300	500	180	180	180
Band gap values **Direct**[a] (eV)	3.22	3.24	3.21	-[b]	3.22	3.26	-[b]	3.21	3.23	3.29	3.32	3.22

Band gap values **Indirect**[a] (eV)	2.77	2.97	2.93	-[b]	2.81	2.99	-[b]	2.72	2.96	3.00	2.98	2.52

[a] Measured with the Tauc method, with a relative error <1%. [b] In the amorphous materials, no band-gap value was measured.

Observing all samples, the band-gap values (Table 2), particularly the direct band-gap values obtained, agree well with the expected E_g of anatase (i.e. $\sim$3.2 eV; $\sim$388 nm) [101], thus the direct allowed model would seem more applicable for these specimens. Anatase, is considered a semiconductor of indirect allowed transition [101], nonetheless, although uncommon, it has been shown that it can have direct transition [102,103]. The slight increase from the 3.2 eV anatase reference value might be due to the presence of small amounts of brookite, that exist in all samples except for T500_CNT. It should be noted that the optical band gap of brookite has been reported to be $\sim$3.4 eV ($\sim$365 nm) [101].

3.2. Photocatalysis (liquid-solid)

The PC ability of the materials was evaluated by their capacity to remove the rhodamine B dye under both UV and visible lights, being the obtained results displayed in Figure 4 and 5, respectively. The variation in concentration of the dye throughout the experiment in also available in ESI (UV and Vis lights, Figures S11 and S12, respectively).

In Figure S11 (ESI), the variation of the RhB concentration (in 7 h) using UV light can be observed. The addition of carbon-based materials did not appear to have a significant effect in mostly of the materials, only improving the material T300_CNT versus its counterparts, at that same temperature, (T300 and T300_GO). This effect was not present in other temperatures (60, 500 and 180 °C), where the sample without carbon (T60, T500 and H180, respectively) had less RhB concentration at the end of the 7 h. These results are not just due to the materials PC ability nor their adsorption but of the interaction between these two phenomena. In S12, the addition of carbon-based materials improved the RhB degradation in some samples. At 60 and 180 °C adding either GO or CNT did not result in less amount of RhB detected after 7h. However, at 300 °C adding either GO or CNT resulted in improved results (over T300). For the sample containing GO and treated at 500 °C, it was observed similar results to that of the sample without any carbon (T500). This was expected since T500_GO material suffered some GO degradation under heating

(Figure S6). Carbon-based materials seem influence more positively RhB degradation when using Vis light instead of UV. It is important to keep in mind, that is not just PC decreasing the amount of RhB but also the adsorption phenomenon, and mainly the interaction between the two phenomena. In different samples each parameter will contribute distinctly to the RhB degradation.

Degradation rates were calculated and are shown for the first 180 min of each reaction using both types of radiation (UV and Vis) in Figures S13 and S14 (ESI), respectively. When using UV light as a radiation source (Figure S13, ESI), the sample T300_CNT has faster kinetics than its homologous temperature samples (T300 and T300_GO). The sample with the highest kinetics is T60 a sample which is mostly amorphous (Figure 1), indicating that, in this sample, adsorption plays a more significant role than photocatalysis in the removal/degradation of RhB. Comparing the degradation rate in UV (Figure S13, ESI) and visible light (Figure S14, ESI) it can be inferred that the highest impact the carbon-based materials have happens with Vis light. At 300 °C, the sample T300_CNT has higher kinetics that the other samples at the same temperature (T300 and T300_GO). The same happened at 180 °C, where H180_CNT has a higher degradation rate then H180 and H180_GO. While at 500 °C, the sample T500_GO degrades the dye faster than both T500 and T500_CNT. Again, T60 has the highest degradation rate assigned to the adsorption phenomenon. In all samples a distinct contribution and balance between the photocatalytic and adsorption phenomena takes place, resulting in these varied degradation rates.

To test the test the materials adsorption ability (Figure 4 and Figure 5) for the first 30 min no light was used (t = 0 to t = 0a), resulting in the first percentage shown in each graph. From t=0a to t=7 both adsorption and photocatalytic abilities are tested in a 7 h interval. The adsorption values (t=0a) of each sample are represented in each graph. Figure 4 shows the RhB degradation under UV light. All pure TiO$_2$ materials show blue shifts, which are a sign of photosensitisation. Photosensitisation is less desirable phenomenon than photocatalysis since it means a slower and incomplete degradation of the dye through continuous N-deethylation of rhodamine B. This process gives, respectively: N,N,N'-triethyl rhodamine peak at 539 nm; N,N'-diethyl rhodamine evidenced by the peak 522 nm, then N-ethyl rhodamine at 510 nm, and finally rhodamine, that has a maximum in absorbance located at 499 nm.[65,104] The blue shifts are more pronounced in T60 and less

in T300, showing the importance of the presence of both crystalline phases anatase and brookite in the later sample (from XRD, Figure 1). The decrease in the amount of blue shift in materials that underwent thermal or hydrothermal treatments shows that these treatments are beneficial in decreasing, in part, the shift. This can be attributed to the formation of the TiO_2 crystalline phases after the temperature treatments, observed in the XRD of the samples (Figure 1). The addition of carbon materials also decreases blue shifts, probably due to an increase in photocatalytic ability due to increase electron transport to TiO_2 and decreased electron-hole recombination [105].
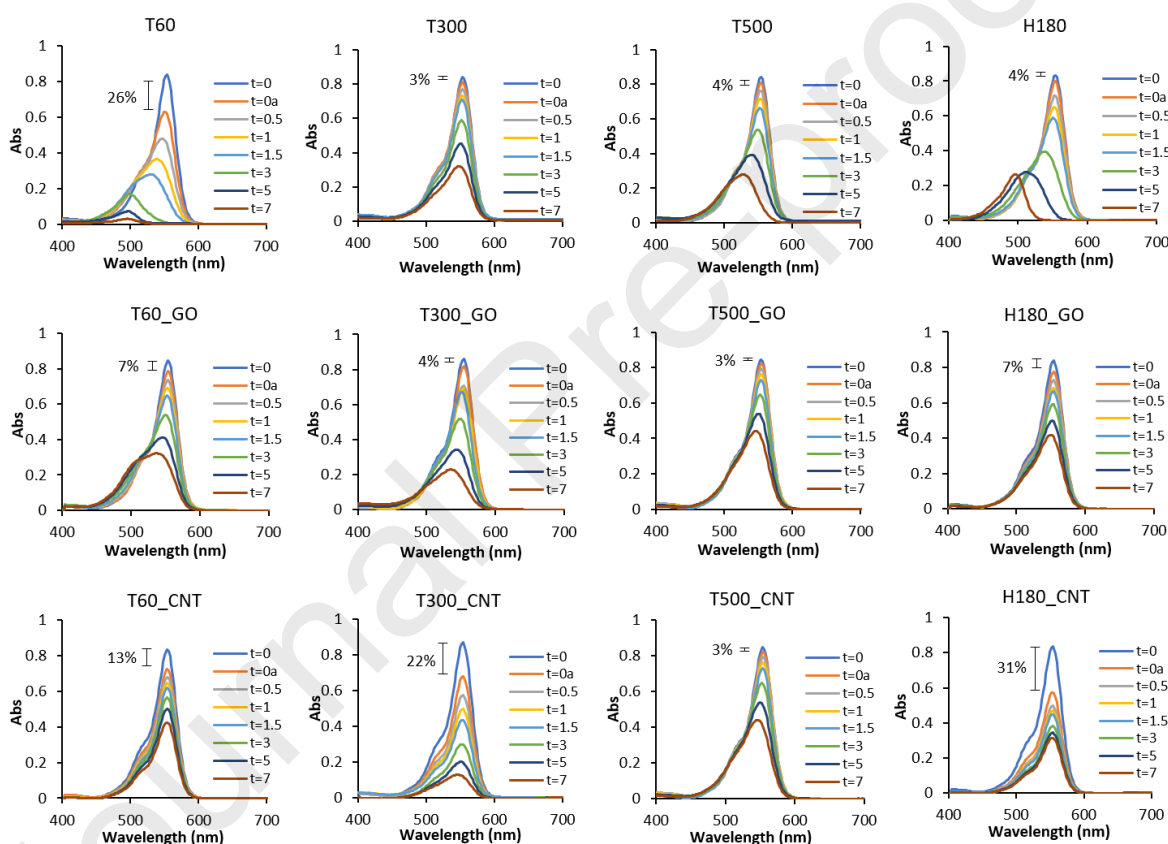

Figure 4. Photocatalytic degradation of the RhB, using UV light during 7 hours, and the Ty(_z) and Hy(_z) samples. The materials adsorption ability percentages (displayed in each graph) were determined by analysing the light absorption at t = 0 and t = 0a corresponding to 30 minutes of aging in absence of light.

The addition of CNT proved to have better results than the GO, with the achievement of no shift in sample T300_CNT aligned with high removal of RhB (83%), through the combined processes of photocatalysis and adsorption.

In Figure 5, the ability of prepared specimens to degrade RhB is patent, but this time with Vis light. The same trend of stronger blue shifts in samples with just TiO_2 is observed and, again, the use of thermal treatments or the carbon (GO or CNT) addition decreased it. In fact, the blue shift is completely absent in the sample T300_CNT under both UV and Vis light. This phenomenon can be attributed to the presence of a higher amount of C and C type used [106], together with the presence of the crystalline phases of TiO_2 (from EA and XRD, Table S1 (ESI) and Figure 1). The material presenting the highest ability to adsorb/degrade RhB under vis-light is once more T300_CNT. Thus, T300_CNT has the ability to degrade RhB in water under both UV and Vis light. To understand which of the processes, adsorption or photocatalytic activity, is more pronounced, the adsorption ability was measured for longer periods of time (7 h) and the result is available in Figure S15 (ESI). It was observed that the T300_CNT has the capacity to adsorb 58% of RhB in 7 h.
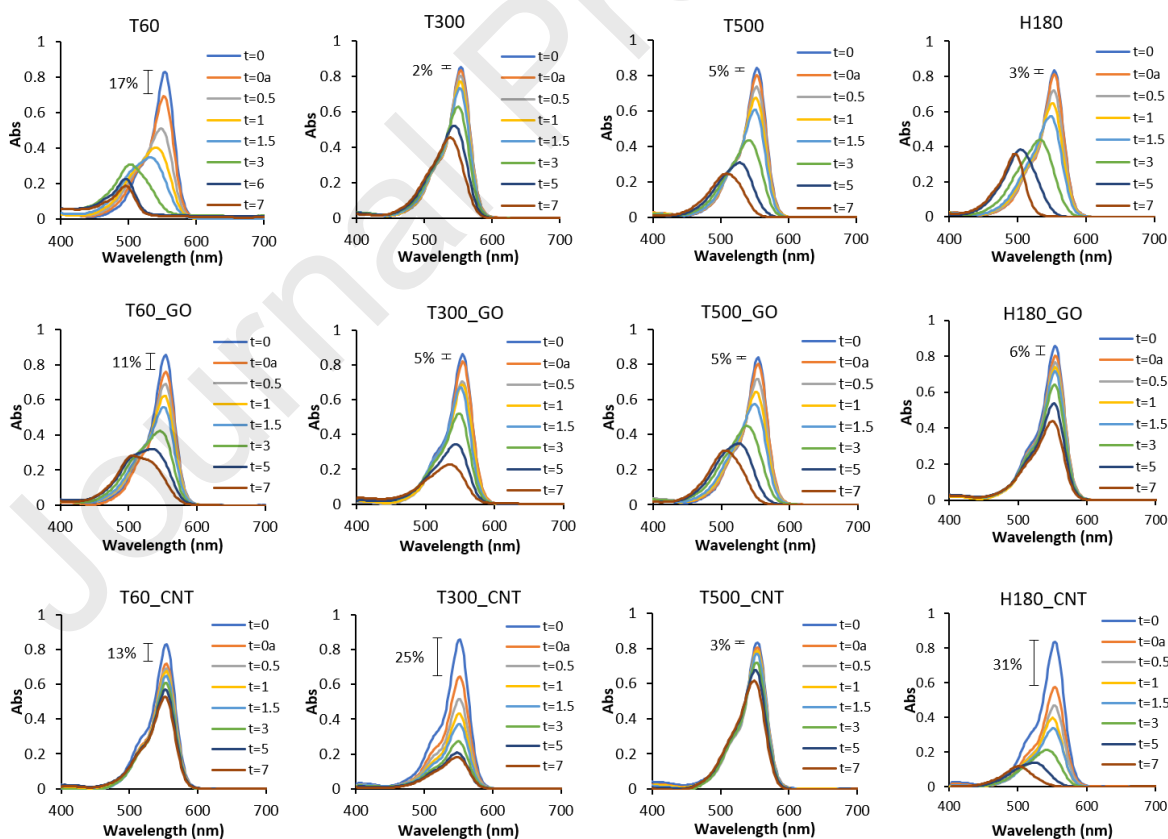
Figure 5. Photocatalytic degradation of the RhB, using Vis light and samples T*y*(*_z*) and H*y*(*_z*). The reaction was followed over 7 hours.

The T300_CNT material was compared with the most used and effective commercial material, P25, using visible and UV light (Figure 6 and Figure S16, ESI). P25 presented a complete photocatalytic degradation of RhB in water under UV light and in the same conditions (Figure S16, ESI), showing a superior performance than all samples synthetized in this study. However, the same result was not observed when the photocatalytic degradation of RhB in water was carried out under vis-light (Figure 6). Unlike what observed with the UV light, the photocatalytic degradation of RhB under Vis light presented a blue shift when P25 catalyst is used, which means that an incomplete removal of the RhB occurred. This result indicates that T300_CNT is more efficient than the commercial Degussa P25 photocatalyst under Vis light.
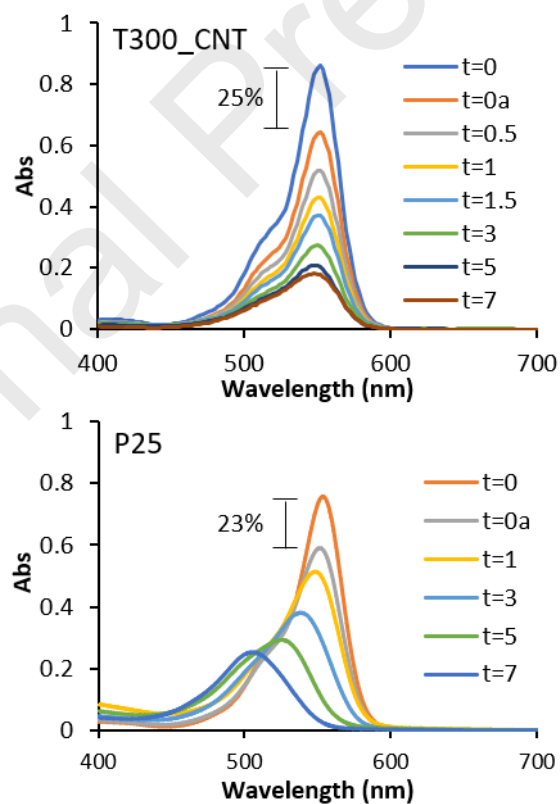
Figure 6. Photocatalytic degradation of the RhB dye using Vis light with the sample T300_CNT (top) and commercial material Degussa P25 (bottom). The reaction was followed over 7 hours,

3.3. Scavenger test

Scavenging tests are used to determine which active species are involved in the decolourization of RhB using Vis light (Figure S17, ESI). The T300_CNT has a degradation rate of 0.037 h^{-1}. Trapping experiments with both IPA and BQ scavenger for •OH and •O^{2-} respectively, had no effect in the photocatalytic activity [107,108]. However, using EDTA as a h$^+$ quencher resulted in a decrease in the degradation rate from 0.037 h^{-1} to 0.026 h^{-1}. This result shows that h$^+$ is the main oxidative species for the N-deethylation of RhB, allowing the decolourization of this dye. The proposed mechanism is described below [109].

When a catalyst absorbs a photon with energy equal to, or higher than the band-gap energy (E_g), electrons (e$^-$) are promoted from the valence band (VB) to the conduction band (CB), leaving an electron vacancy or hole (h$_{VB}^+$) in the VB, and these reactions happens in its surface, as shown in Equations 1–4.

$$\text{T300\_CNT} + h\nu \rightarrow \text{e}_{CB}^- + \text{h}_{VB}^+ \qquad \text{(Equation 1)}$$
$$\text{h}_{VB}^+ + \text{H}_2\text{O}_{(ads)} \rightarrow {}^{\bullet}\text{OH}_{(ads)} + \text{H}^+ \qquad \text{(Equation 2)}$$
$$\text{e}_{CB}^- + \text{O}_{2(ads)} \rightarrow {}^{\bullet}\text{O}_{2(ads)}^- \qquad \text{(Equation 3)}$$
$$\text{e}_{CB}^- + \text{h}_{VB}^+ \rightarrow \text{energy} \qquad \text{(Equation 4)}$$

From the trapping experiments described above, it is known that h$_{VB}^+$ quenching had an adverse effect on the reaction. It can thus speculate that they probably did not allow for the formation of •OH adequate to oxidize RhB (see Equation 5), therefore lowering the reaction kinetic.

$\cdot OH_{(ads)} + RhB \rightarrow$ degradation products $\hspace{4cm}$ (5)
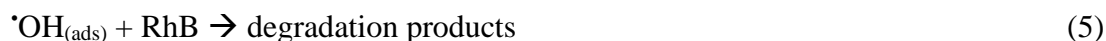
Photocatalysis (gas-solid)

The photocatalytic activity of the most promising materials (T300, T300_GO and T300_CNT) are also evaluated in the degradation of benzene (Figure **7**) using solar light and compared with the commercial sample Degussa P25.
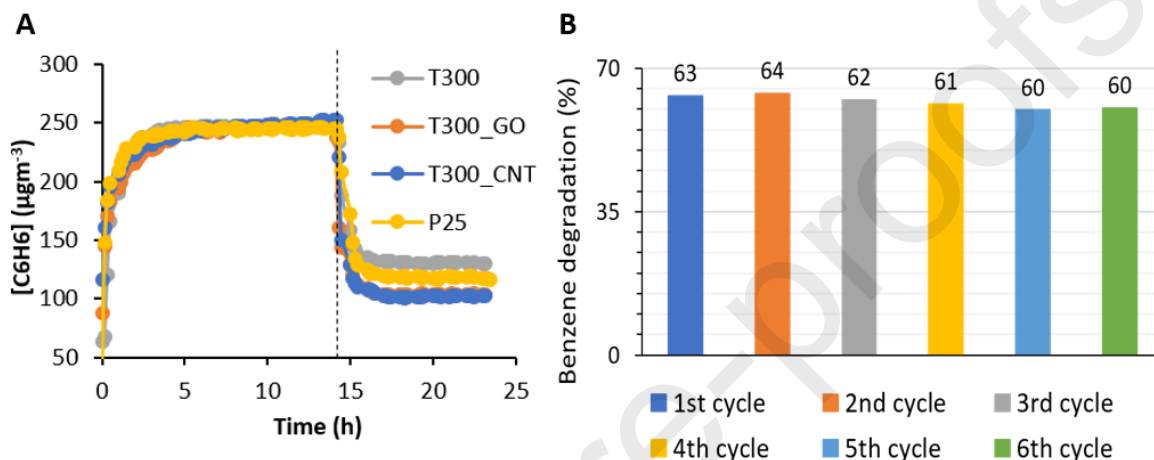

Figure 7. A- Photocatalytic removal of benzene. The vertical dashed line shows the time at which the solar light was turned on. B- Re-usability test of T300_CNT in 6 cycles.

The samples T300_CNT and T300_GO showed a benzene removal of 59.3 and 58.4% respectively, which is higher than that observed for P25 (52.6%) and for the parent T300 (48.0%). These results clearly convey the improvements provided by the addition of carbon materials as well as show the potential these materials to remove pollutants from the air. This outcome could be a consequence of enhanced electronic transport and reduced electron-hole recombination [55], provided by the carbon materials' addition.

Figure 7B shows the re-usability of the most promising sample, T300_CNT, in the photocatalytic removal of benzene under solar light. It can be observed that the T300_CNT material maintained high photocatalytic ability after 6 cycles.

4. CONCLUSIONS

Titanium dioxide and titanium dioxide-based materials were thermally treated at different temperatures and pressures resulting in materials with distinct physical properties, mineralogical phases composition and, consequently, different photocatalytic abilities.

The use of thermal treatment at 500 ºC in samples with GO and CNT resulted in the degradation of the carbon materials, which was proved by TGA. The increase of temperature of the thermally treated (T) materials leads to a decrease of their specific surface area which was associated to the collapse of the pores. The hydrothermal treatment (H) resulted in pore collapse and lower surface areas. This is proven by the lower surface areas of H samples than samples T300 (300 ºC), despite being made at a lower temperature (180 ºC).

The band-gap results show that a direct allowed model for electron movement is applicable for all the materials.

Regarding the material's adsorption ability, T300_CNT material greatly adsorbed RhB, augmented the contact time between pollutant and photocatalytic material and therefore, possibly increasing the photocatalytic degradation rates. As for the photocatalytic ability of the materials in the degradation of RhB, the use of both GO and CNT brought added value to the TiO_2, as they reduce the blue shift behaviour of the samples, increasing instead photocatalysis. The T300_CNT material had the highest RhB degradation ability, under both UV and visible light, through simultaneous adsorption and photocatalysis processes. The comparison between T300_CNT and commercial P25 showed that the former material has superior ability in the degradation of RhB under visible light. Regarding photocatalysis in gas medium, using benzene as pollutant model, T300_GO and T300_CNT showed better results than the commercial P25 under solar light. The better photocatalytic performance of T300_CNT can be explained by the high surface area and the carbon content (highest of all crystalline materials produced), lowest band gap and it also had the advantages brought by the use of carbon nanotubes namely: reduced electron-hole recombination and enhanced electronic transport. Moreover, T300_CNT maintained, after 6 cycles, its ability to degrade benzene. From the overall results, the high photocatalytic ability of T300_CNT material and its reusability together with its simple preparation make this material highly interesting

for its potential application in cyclic photocatalytic degradation of organic pollutants under UV-A, Vis and solar light in both aqueous and gas medium.

FOOTNOTES

Electronic supplementary information (ESI) available: Materials characterization details and further data from XRD, -196 °C N_2-sorption isotherms, EA, SEM, UHRTEM, RAMAN spectroscopy, TGA, XPS, the variation in concentration of the RhB throughout the experiment for all materials and photocatalytic degradation experiments for P25.

AUTHOR CONTRIBUTIONS

The manuscript was written through contributions of all authors. All authors have given approval to the final version of the manuscript.

ACNOWLEDGEMENT

REFERENCES

[1]   M. Ritchie, Hannah; Roser, Air Pollution, Ourworldindata.Org. (2017). https://ourworldindata.org/air-pollution#exposure-to-particulate-matter   (accessed November 23, 2018).

[2]   UNESCO, The United Nations World Water Development report 2017, 2017.

[3]   D. Eugenio, Rodriguez Natalia; Mclaughlin; Pennock, Soil pollution: a hidden reality, Rome, FAO (2018) 142 pp.

[4]   W.-H. Leung, W.-H. Lo, P.-H. Chan, Amyloid fibrils as rapid and efficient nano-biosorbents for removal of dye pollutants, RSC Adv. 5 (2015) 90022–90030. doi:10.1039/C5RA17182B.

[5]   K.-C. Chen, J.-Y. Wu, D.-J. Liou, S.-C.J. Hwang, Decolorization of the textile dyes by newly isolated bacterial strains, J. Biotechnol. 101 (2003) 57–68. doi:10.1016/S0168-1656(02)00303-6.

[6]   R. Kant, Textile dyeing industry an environmental hazard, Nat. Sci. 04 (2012) 22–26. doi:10.4236/ns.2012.41004.

[7]   S. Wijannarong, S. Aroonsrimorakot, P. Thavipoke, charaporn Kumsopa, S. Sangjan, Removal of Reactive Dyes from Textile Dyeing Industrial Effluent by Ozonation Process, APCBEE Procedia. 5 (2013) 279–282. doi:10.1016/j.apcbee.2013.05.048.

[8]   F.M.M. Paschoal, M.A. Anderson, M.V.B. Zanoni, Simultaneous removal of chromium and leather dye from simulated tannery effluent by photoelectrochemistry, J. Hazard. Mater. 166 (2009) 531–537. doi:10.1016/j.jhazmat.2008.11.058.

[9]   S. Agarwal, S. Yadav, A. Sharma, K. Singh, A.B. Gupta, Kinetic and equilibrium studies of decolorization of effluent of handmade paper industry by low-cost fly ash, Desalin. Water Treat. 57 (2016) 25783–25799. doi:10.1080/19443994.2016.1157764.

[10] G. Felix, N. Thomas, Evidence of two effects in the size segregation process in a dry granular media, Food Chem. Toxicol. 42 (2004) 517–543.

doi:10.1103/PhysRevE.70.051307.

[11] F.O. Topaç-Şağban, E. Dindar, S. Uçaroğlu, H.S. Başkaya, Biostimulation of Azo Dye-Contaminated Soils by Food Industry Sludge, Soil Sediment Contam. An Int. J. 19 (2010) 436–454. doi:10.1080/15320383.2010.486055.

[12] Z. Carmen, S. Daniel, Textile Organic Dyes – Characteristics, Polluting Effects and Separation/Elimination Procedures from Industrial Effluents – A Critical Overview, in: Org. Pollut. Ten Years After Stock. Conv. - Environ. Anal. Updat., InTech, 2012: pp. 55–56. doi:10.5772/32373.

[13] S. Dawood, T.K. Sen, Removal of anionic dye Congo red from aqueous solution by raw pine and acid-treated pine cone powder as adsorbent: Equilibrium, thermodynamic, kinetics, mechanism and process design, Water Res. 46 (2012) 1933–1946. doi:10.1016/j.watres.2012.01.009.

[14] X. Xu, H. Li, W. Wang, J. Gu, Decolorization of dyes and textile wastewater by potassium permanganate, Chemosphere. 59 (2005) 893–898. doi:10.1016/j.chemosphere.2004.11.013.

[15] M.A. Hassaan, A. El Nemr, Health and Environmental Impacts of Dyes : Mini Review, Am. J. Environ. Sci. Eng. 1 (2017) 64–67. doi:10.11648/j.ajese.20170103.11.

[16] M. Oplatowska, R.F. Donnelly, R.J. Majithiya, D. Glenn Kennedy, C.T. Elliott, The potential for human exposure, direct and indirect, to the suspected carcinogenic triphenylmethane dye Brilliant Green from green paper towels, Food Chem. Toxicol. 49 (2011) 1870–1876. doi:10.1016/j.fct.2011.05.005.

[17] R.W. Sabnis, Handbook of Biological Dyes and Stains, Wiley, Hoboken, NJ, USA, 2010. doi:10.1002/9780470586242.

[18] K. SARAYU, K. SWAMINATHAN, S. SANDHYA, Assessment of degradation of eight commercial reactive azo dyes individually and in mixture in aqueous solution by ozonation, Dye. Pigment. 75 (2007) 362–368. doi:10.1016/j.dyepig.2006.06.011.

[19] M. Pedrosa, L.M. Pastrana-Martínez, M.F.R. Pereira, J.L. Faria, J.L. Figueiredo, A.M.T. Silva, N/S-doped graphene derivatives and TiO 2 for catalytic ozonation and photocatalysis of water pollutants, Chem. Eng. J. 348 (2018) 888–897. doi:10.1016/j.cej.2018.04.214.

[20] B. Vahid, T. Mousanejad, A. Khataee, Sonocatalytic ozonation, with nano-TiO2 as catalyst, for degradation of 4-chloronitrobenzene in aqueous solution, Res. Chem. Intermed. 41 (2015) 7029–7042. doi:10.1007/s11164-014-1796-1.

[21] E. Isarain-Chávez, M.D. Baró, E. Rossinyol, U. Morales-Ortiz, J. Sort, E. Brillas, E. Pellicer, Comparative electrochemical oxidation of methyl orange azo dye using Ti/Ir-Pb, Ti/Ir-Sn, Ti/Ru-Pb, Ti/Pt-Pd and Ti/RuO 2 anodes, Electrochim. Acta. 244 (2017) 199–208. doi:10.1016/j.electacta.2017.05.101.

[22] S. Mohana, S. Shrivastava, J. Divecha, D. Madamwar, Response surface methodology for optimization of medium for decolorization of textile dye Direct Black 22 by a novel bacterial consortium, Bioresour. Technol. 99 (2008) 562–569. doi:10.1016/j.biortech.2006.12.033.

[23] K. Svobodová, M. Senholdt, Č. Novotný, A. Rehorek, Mechanism of Reactive Orange 16 degradation with the white rot fungus Irpex lacteus, Process Biochem. 42 (2007) 1279–1284. doi:10.1016/j.procbio.2007.06.002.

[24] A.B. Albadarin, C. Mangwandi, Mechanisms of Alizarin Red S and Methylene blue biosorption onto olive stone by-product: Isotherm study in single and binary systems, J. Environ. Manage. 164 (2015) 86–93.

doi:10.1016/j.jenvman.2015.08.040.

[25]   F. Vafaei, A. Movafeghi, A. Khataee, Evaluation of antioxidant enzymes activities and identification of intermediate products during phytoremediation of an anionic dye (C.I. Acid Blue 92) by pennywort (Hydrocotyle vulgaris), J. Environ. Sci. (China). 25 (2013) 2214–2222. doi:10.1016/S1001-0742(12)60306-4.

[26]   S. Sirohi, A. Singh, C. Dagar, G. Saini, B. Pani, R. Nain, Facile synthesis of microporous SiO2/triangular Ag composite nanostructures for photocatalysis, Appl. Nanosci. 7 (2017) 633–643. doi:10.1007/s13204-017-0597-4.

[27]   M. Shahnas Beegam, S.B. Narendranath, P. Periyat, Tuning of selective solar photocatalysis by Mn 2+ decorated nanocrystalline mesoporous TiO 2, Sol. Energy. 158 (2017) 774–781. doi:10.1016/j.solener.2017.10.046.

[28]   J. Pan, L. Guo, S. Zhang, N. Wang, S. Jin, B. Tan, Embedding Carbon Nitride into a Covalent Organic Framework with Enhanced Photocatalysis Performance, Chem. - An Asian J. 13 (2018) 1674–1677. doi:10.1002/asia.201800506.

[29]   R. Das, Application Photocatalysis for Treatment of Industrial Waste Water—A Short Review, OALib. 01 (2014) 1–17. doi:10.4236/oalib.1100713.

[30]   M.L. Boeglin, D. Wessels, D. Henshel, An investigation of the relationship between air emissions of volatile organic compounds and the incidence of cancer in Indiana counties, Environ. Res. 100 (2006) 242–254. doi:10.1016/j.envres.2005.04.004.

[31]   M.A. D'Andrea, G.K. Reddy, Adverse Health Complaints of Adults Exposed to Benzene After a Flaring Disaster at the BP Refinery Facility in Texas City, Texas, Disaster Med. Public Health Prep. 12 (2018) 232–240. doi:10.1017/dmp.2017.59.

[32]   A.E. Janitz, J.E. Campbell, S. Magzamen, A. Pate, J.A. Stoner, J.D. Peck, Benzene and childhood acute leukemia in Oklahoma, Environ. Res. 158 (2017) 167–173.

doi:10.1016/j.envres.2017.06.015.

[33]   F.M. Carlos-Wallace, L. Zhang, M.T. Smith, G. Rader, C. Steinmaus, Parental, In Utero, and Early-Life Exposure to Benzene and the Risk of Childhood Leukemia: A Meta-Analysis, Am. J. Epidemiol. 183 (2016) 1–14. doi:10.1093/aje/kwv120.

[34]   O.J. Adegoke, A. Blair, X.O. Shu, M. Sanderson, F. Jin, M. Dosemeci, C.L. Addy, W. Zheng, Occupational history and exposure and the risk of adult leukemia in Shanghai, Ann. Epidemiol. 13 (2003) 485–494. doi:10.1016/S1047-2797(03)00037-1.

[35]   H.D. Rad, A.A. Babaei, G. Goudarzi, K.A. Angali, Z. Ramezani, M.M. Mohammadi, Levels and sources of BTEX in ambient air of Ahvaz metropolitan city, Air Qual. Atmos. Heal. 7 (2014) 515–524. doi:10.1007/s11869-014-0254-y.

[36]   J. Bender, H.-J. Weigel, Changes in atmospheric chemistry and crop health: A review, Agron. Sustain. Dev. 31 (2011) 81–89. doi:10.1051/agro/2010013.

[37]   W.H.O. (WHO), IARC (International Agency for Research on Cancer), 1982. Some industrial chemicals and dyestuffs, Vol. 29. In: IARC Monographs on the Evaluation of the Carcinogenic Risk of Chemicals to Humans. Lyon, p. 416., 2016.

[38]   K.-J. Oh, D.-W. Park, S.-S. Kim, S.-W. Park, Breakthrough data analysis of adsorption of volatile organic compounds on granular activated carbon, Korean J. Chem. Eng. 27 (2010) 632–638. doi:10.1007/s11814-010-0079-9.

[39]   G. Zhou, X. He, S. Liu, H. Xie, M. Fu, Phenyl VOCs catalytic combustion on supported CoMn/AC oxide catalyst, J. Ind. Eng. Chem. 21 (2015) 932–941. doi:10.1016/j.jiec.2014.04.035.

[40]   C.W. Ahn, Y.W. You, I. Heo, J.S. Hong, J.K. Jeon, Y.D. Ko, Y.H. Kim, H. Park, J.K. Suh, Catalytic combustion of volatile organic compound over spherical-shaped

copper–manganese oxide, J. Ind. Eng. Chem. 47 (2017) 439–445. doi:10.1016/j.jiec.2016.12.018.

[41] P. Morales, M. Cáceres, F. Scott, L. Díaz-Robles, G. Aroca, A. Vergara-Fernández, Biodegradation of benzo[α]pyrene, toluene, and formaldehyde from the gas phase by a consortium of Rhodococcus erythropolis and Fusarium solani, Appl. Microbiol. Biotechnol. 101 (2017) 6765–6777. doi:10.1007/s00253-017-8400-8.

[42] V.S. Priya, L. Philip, Treatment of volatile organic compounds in pharmaceutical wastewater using submerged aerated biological filter, Chem. Eng. J. 266 (2015) 309–319. doi:10.1016/j.cej.2014.12.048.

[43] G. Liu, J. Ji, H. Huang, R. Xie, Q. Feng, Y. Shu, Y. Zhan, R. Fang, M. He, S. Liu, X. Ye, D.Y.C. Leung, UV/H 2 O 2 : An efficient aqueous advanced oxidation process for VOCs removal, Chem. Eng. J. 324 (2017) 44–50. doi:10.1016/j.cej.2017.04.105.

[44] M. Sleiman, P. Conchon, C. Ferronato, J.-M. Chovelon, Photocatalytic oxidation of toluene at indoor air levels (ppbv): Towards a better assessment of conversion, reaction intermediates and mineralization, Appl. Catal. B Environ. 86 (2009) 159–165. doi:10.1016/j.apcatb.2008.08.003.

[45] A.H. Mamaghani, F. Haghighat, C.-S. Lee, Photocatalytic degradation of VOCs on various commercial titanium dioxides: Impact of operating parameters on removal efficiency and by-products generation, Build. Environ. 138 (2018) 275–282. doi:10.1016/j.buildenv.2018.05.002.

[46] W.R. Siah, H.O. Lintang, M. Shamsuddin, L. Yuliati, High photocatalytic activity of mixed anatase-rutile phases on commercial TiO_2 nanoparticles, IOP Conf. Ser. Mater. Sci. Eng. 107 (2016) 012005 (1-8). doi:10.1088/1757-899X/107/1/012005.

[47] J.G. Yu, Y.R. Su, B. Cheng, Template-Free Fabrication and Enhanced Photocatalytic

Activity of Hierarchical Macro-/Mesoporous Titania, Adv. Funct. Mater. 17 (2007) 1984–1990. doi:10.1002/adfm.200600933.

[48]   M. Cargnello, T.R. Gordon, C.B. Murray, Solution-Phase Synthesis of Titanium Dioxide Nanoparticles and Nanocrystals, Chem. Rev. 114 (2014) 9319–9345. doi:10.1021/cr500170p.

[49]   A.G. R Ananthashankar, Production, Characterization and Treatment of Textile Effluents: A Critical Review, J. Chem. Eng. Process Technol. 05 (2013) 1–18. doi:10.4172/2157-7048.1000182.

[50]   A. Pimentel, D. Nunes, S. Pereira, R. Martins, E. Fortunato, Photocatalytic Activity of TiO2 Nanostructured Arrays Prepared by Microwave-Assisted Solvothermal Method, in: Semicond. Photocatal. - Mater. Mech. Appl., InTech, 2016: pp. 81–103. doi:10.5772/63237.

[51]   S.B.A. Hamid, T.L. Tan, C.W. Lai, E.M. Samsudin, Multiwalled carbon nanotube/TiO_2 nanocomposite as a highly active photocatalyst for photodegradation of Reactive Black 5 dye, Chinese J. Catal. 35 (2014) 2014–2019. doi:10.1016/S1872-2067(14)60210-2.

[52]   X. Chen, C. Burda, The electronic origin of the visible-light absorption properties of C- , N- and S-doped TiO_2 nanomaterials the electronic origin of the visible-light absorption, J. Am. Chem. Socitey. 130 (2008) 5018–5019. doi:10.1021/ja711023z.

[53]   J.F. Guayaquil-Sosa, B. Serrano-Rosales, P.J. Valadés-Pelayo, H. de Lasa, Photocatalytic hydrogen production using mesoporous TiO_2 doped with Pt, Appl. Catal. B Environ. 211 (2017) 337–348. doi:10.1016/j.apcatb.2017.04.029.

[54]   M. Raffi, Z. Batool, M. Ahmad, M. Zakria, R.I. Shakoor, M.A. Mirza, A. Mahmood, Synthesis of Ag-Loaded TiO_2 Electrospun Nanofibers for Photocatalytic

Decolorization of Methylene Blue, Fibers Polym. 19 (2018) 1930–1939. doi:10.1007/s12221-018-8227-7.

[55] Y. Huang, D. Chen, X. Hu, Y. Qian, D. Li, Preparation of TiO2/Carbon Nanotubes/Reduced Graphene Oxide Composites with Enhanced Photocatalytic Activity for the Degradation of Rhodamine B, Nanomaterials. 8 (2018) 431. doi:10.3390/nano8060431.

[56] P. Daram, C. Banjongprasert, W. Thongsuwan, S. Jiansirisomboon, Microstructure and photocatalytic activities of thermal sprayed titanium dioxide/carbon nanotubes composite coatings, Surf. Coatings Technol. 306 (2016) 290–294. doi:10.1016/j.surfcoat.2016.06.068.

[57] M. Cruz, C. Gomez, C.J. Duran-Valle, L.M. Pastrana-Martínez, J.L. Faria, A.M.T. Silva, M. Faraldos, A. Bahamonde, Bare TiO_2 and graphene oxide TiO_2 photocatalysts on the degradation of selected pesticides and influence of the water matrix, Appl. Surf. Sci. 416 (2017) 1013–1021. doi:10.1016/j.apsusc.2015.09.268.

[58] J. Jing, Y. Zhang, W. Li, W.W. Yu, Visible light driven photodegradation of quinoline over TiO_2/graphene oxide nanocomposites, J. Catal. 316 (2014) 174–181. doi:10.1016/j.jcat.2014.05.009.

[59] A.W. Morawski, E. Kusiak-Nejman, A. Wanag, J. Kapica-Kozar, R.J. Wróbel, B. Ohtani, M. Aksienionek, L. Lipińska, Photocatalytic degradation of acetic acid in the presence of visible light-active TiO_2 -reduced graphene oxide photocatalysts, Catal. Today. 280 (2017) 108–113. doi:10.1016/j.cattod.2016.05.055.

[60] J. Yao, H. Chen, F. Jiang, Z. Jiao, M. Jin, Titanium dioxide and cadmium sulfide co-sensitized graphitic carbon nitride nanosheets composite photocatalysts with superior performance in phenol degradation under visible-light irradiation, J. Colloid

Interface Sci. 490 (2017) 154–162. doi:10.1016/j.jcis.2016.11.051.

[61] L. Matějová, M. Šihor, J. Lang, I. Troppová, N. Ambrožová, M. Reli, T. Brunátová, L. Čapek, A. Kotarba, K. Kočí, Investigation of low Ce amount doped-TiO_2 prepared by using pressurized fluids in photocatalytic N_2O decomposition and CO_2 reduction, J. Sol-Gel Sci. Technol. 84 (2017) 158–168. doi:10.1007/s10971-017-4464-2.

[62] R.P. Vitiello, J.M. Macak, A. Ghicov, H. Tsuchiya, L.F.P. Dick, P. Schmuki, N-Doping of anodic TiO_2 nanotubes using heat treatment in ammonia, Electrochem. Commun. 8 (2006) 544–548. doi:10.1016/j.elecom.2006.01.023.

[63] X. Yan, K. Yuan, N. Lu, H. Xu, S. Zhang, N. Takeuchi, H. Kobayashi, R. Li, The interplay of sulfur doping and surface hydroxyl in band gap engineering: Mesoporous sulfur-doped TiO_2 coupled with magnetite as a recyclable, efficient, visible light active photocatalyst for water purification, Appl. Catal. B Environ. 218 (2017) 20–31. doi:10.1016/j.apcatb.2017.06.022.

[64] H. Liang, Z. Jia, H. Zhang, X. Wang, J. Wang, Photocatalysis oxidation activity regulation of Ag/TiO_2 composites evaluated by the selective oxidation of Rhodamine B, Appl. Surf. Sci. 422 (2017) 1–10. doi:10.1016/j.apsusc.2017.05.211.

[65] M. Rochkind, S. Pasternak, Y. Paz, Using Dyes for Evaluating Photocatalytic Properties: A Critical Review, Molecules 20 (2014) 88–110. doi:10.3390/molecules20010088.

[66] D.C. Marcano, D. V. Kosynkin, J.M. Berlin, A. Sinitskii, Z. Sun, A. Slesarev, L.B. Alemany, W. Lu, J.M. Tour, Improved Synthesis of Graphene Oxide, ACS Nano. 4 (2010) 4806–4814. doi:10.1021/nn1006368.

[67] Y. Chai, J. Ding, L. Wang, Q. Liu, J. Ren, W. Dai, Applied Catalysis B : Environmental Enormous enhancement in photocatalytic performance of Ag_3PO_4 /

HAp composite : A Z-scheme mechanism insight, Applied Catal. B, Environ. 179 (2015) 29–36. doi:10.1016/j.apcatb.2015.05.006.

[68] D.M. Tobaldi, L. Lajaunie, M. López Haro, R.A.S. Ferreira, M. Leoni, M.P. Seabra, J.J. Calvino, L.D. Carlos, J.A. Labrincha, Synergy of Neodymium and Copper for Fast and Reversible Visible-light Promoted Photochromism, and Photocatalysis, in Cu/Nd-TiO$_2$ Nanoparticles, ACS Appl. Energy Mater. 2 (2019) 3237–3252. doi:10.1021/acsaem.9b00084.

[69] W.H.O. (WHO), Guidelines for Indoor Air Quality: Selected Pollutants, 2010, (2010). www.euro.who.int/__data/assets/pdf_file/0009/128169/e94535.pdf (accessed May 28, 2019).

[70] U. Ibrahim, A. Halim, Heterogeneous photocatalytic degradation of organic contaminants over titanium dioxide : A review of fundamentals , progress and problems, J. Photochem. Photobiol. C Photochem. Rev. 9 (2008) 1–12. doi:10.1016/j.jphotochemrev.2007.12.003.

[71] C.C.N. de Melo, C.A.G. Beatrice, L.A. Pessan, A.D. de Oliveira, F.M. Machado, Analysis of nonisothermal crystallization kinetics of graphene oxide - reinforced polyamide 6 nanocomposites, Thermochim. Acta. 667 (2018) 111–121. doi:10.1016/j.tca.2018.07.014.

[72] A.B. Kaganj, A.M. Rashidi, R. Arasteh, S. Taghipoor, Crystallisation behaviour and morphological characteristics of poly(propylene)/multi-walled carbon nanotube nanocomposites, J. Exp. Nanosci. 4 (2009) 21–34. doi:10.1080/17458080802688427.

[73] M. Thommes, K. Kaneko, A. V. Neimark, J.P. Olivier, F. Rodriguez-Reinoso, J. Rouquerol, K.S.W. Sing, Physisorption of gases, with special reference to the

evaluation of surface area and pore size distribution (IUPAC Technical Report), Pure Appl. Chem. 87 (2015) 1051–1069. doi:10.1515/pac-2014-1117.

[74] M.A.O. Lourenço, M.L. Pinto, J. Pires, J.R.B. Gomes, P. Ferreira, Carbonization of periodic mesoporous phenylene- and biphenylene-silicas for CO_2/CH_4 separation, Carbon N. Y. 119 (2017) 267–277. doi:10.1016/j.carbon.2017.04.029.

[75] J. Yu, M. Zhou, B. Cheng, H. Yu, X. Zhao, Ultrasonic preparation of mesoporous titanium dioxide nanocrystalline photocatalysts and evaluation of photocatalytic activity, J. Mol. Catal. A Chem. 227 (2005) 75–80. doi:10.1016/j.molcata.2004.10.012.

[76] R. Krishnapriya, S. Praneetha, A. Vadivel Murugan, Microwave-solvothermal synthesis of various TiO_2 nano-morphologies with enhanced efficiency by incorporating Ni nanoparticles in an electrolyte for dye-sensitized solar cells, Inorg. Chem. Front. 4 (2017) 1665–1678. doi:10.1039/C7QI00329C.

[77] U. Balachandran, N.G. Eror, Raman spectra of titanium dioxide, J. Solid State Chem. 42 (1982) 276–282. doi:10.1016/0022-4596(82)90006-8.

[78] G.A. Tompsett, G.A. Bowmaker, R.P. Cooney, J.B. Metson, K.A. Rodgers, J.M. Seakins, The Raman spectrum of brookite, TiO_2 (Pbca, $Z = 8$), J. Raman Spectrosc. 26 (1995) 57–62. doi:10.1002/jrs.1250260110.

[79] J.S. Mehta, A.C. Faucett, A. Sharma, J.M. Mativetsky, How Reliable Are Raman Spectroscopy Measurements of Graphene Oxide?, J. Phys. Chem. C. 121 (2017) 16584–16591. doi:10.1021/acs.jpcc.7b04517.

[80] Z. Ni, Y. Wang, T. Yu, Z. Shen, Raman spectroscopy and imaging of graphene, Nano Res. 1 (2008) 273–291. doi:10.1007/s12274-008-8036-1.

[81] M.S. Dresselhaus, G. Dresselhaus, R. Saito, A. Jorio, Raman spectroscopy of carbon

nanotubes, Phys. Rep. 409 (2005) 47–99. doi:10.1016/j.physrep.2004.10.006.

[82] A. Mahajan, A. Kingon, Á. Kukovecz, Z. Konya, P.M. Vilarinho, Studies on the thermal decomposition of multiwall carbon nanotubes under different atmospheres, Mater. Lett. 90 (2013) 165–168. doi:10.1016/j.matlet.2012.08.120.

[83] I. Sengupta, S. Chakraborty, M. Talukdar, S.K. Pal, S. Chakraborty, Thermal reduction of graphene oxide: How temperature influences purity, J. Mater. Res. 33 (2018) 4113–4122. doi:10.1557/jmr.2018.338.

[84] P. Wang, S. Zhan, Y. Xia, S. Ma, Q. Zhou, Y. Li, The fundamental role and mechanism of reduced graphene oxide in rGO/Pt-TiO2 nanocomposite for high-performance photocatalytic water splitting, Appl. Catal. B Environ. 207 (2017) 335–346. doi:10.1016/j.apcatb.2017.02.031.

[85] L.A.A. Rodríguez, M. Pianassola, D.N. Travessa, Production of TiO2 Coated Multiwall Carbon Nanotubes by the Sol-Gel Technique, Mater. Res. 20 (2017) 96–103. doi:10.1590/1980-5373-mr-2017-0406.

[86] A. Saha, A. Moya, A. Kahnt, D. Iglesias, S. Marchesan, R. Wannemacher, M. Prato, J.J. Vilatela, D.M. Guldi, Interfacial charge transfer in functionalized multi-walled carbon nanotube@TiO 2 nanofibres, Nanoscale. 9 (2017) 7911–7921. doi:10.1039/C7NR00759K.

[87] L. Karimi, M.E. Yazdanshenas, R. Khajavi, A. Rashidi, M. Mirjalili, Using graphene/TiO2 nanocomposite as a new route for preparation of electroconductive, self-cleaning, antibacterial and antifungal cotton fabric without toxicity, Cellulose. 21 (2014) 3813–3827. doi:10.1007/s10570-014-0385-1.

[88] J. Marques Neto, C. Bellato, C. de Souza, R. da Silva, P. Rocha, Synthesis, Characterization and Enhanced Photocatalytic Activity of Iron Oxide/Carbon

Nanotube/Ag-doped TiO_2 Nanocomposites, J. Braz. Chem. Soc. 28 (2017) 2301–2312. doi:10.21577/0103-5053.20170081.

[89] S. Kumari, A. Shekhar, D.D. Pathak, Graphene oxide–TiO_2 composite: an efficient heterogeneous catalyst for the green synthesis of pyrazoles and pyridines, New J. Chem. 40 (2016) 5053–5060. doi:10.1039/C5NJ03380B.

[90] P. Ribao, M.J. Rivero, I. Ortiz, TiO_2 structures doped with noble metals and/or graphene oxide to improve the photocatalytic degradation of dichloroacetic acid, Environ. Sci. Pollut. Res. 24 (2017) 12628–12637. doi:10.1007/s11356-016-7714-x.

[91] F. Ghasemi, S. Kimiagar, M. Shahbazi, H. Vojoudi, Removel enhancement of basic Blue 41 by rGO–TiO_2 nanocomposite synthesized using pulsed laser, Surf. Rev. Lett. 25 (2018) 1850041–1850048. doi:10.1142/S0218625X18500415.

[92] S. Wang, J. Zhu, Y. Rao, B. Li, S. Zhao, H. Bai, J. Cui, Polydopamine Modified Graphene Oxide-TiO2 Nanofiller for Reinforcing Physical Properties and Anticorrosion Performance of Waterborne Epoxy Coatings, Appl. Sci. 9 (2019) 3760. doi:10.3390/app9183760.

[93] B. Bharti, S. Kumar, H.-N. Lee, R. Kumar, Formation of oxygen vacancies and Ti3+ state in TiO_2 thin film and enhanced optical properties by air plasma treatment, Sci. Rep. 6 (2016) 32355. doi:10.1038/srep32355.

[94] H. Cao, F. Qi, X. Ouyang, N. Zhao, Y. Zhou, B. Li, W. Luo, B. Liao, J. Luo, Effect of Ti Transition Layer Thickness on the Structure, Mechanical and Adhesion Properties of Ti-DLC Coatings on Aluminum Alloys, Materials (Basel). 11 (2018) 1742. doi:10.3390/ma11091742.

[95] G. Rajender, J. Kumar, P.K. Giri, Interfacial charge transfer in oxygen deficient TiO_2-graphene quantum dot hybrid and its influence on the enhanced visible light

photocatalysis, Appl. Catal. B Environ. 224 (2018) 960–972. doi:10.1016/j.apcatb.2017.11.042.

[96] A. Mezni, N. Ben Saber, M.M. Ibrahim, M. El-Kemary, A. Aldalbahi, P. Feng, L. Samia Smiri, T. Altalhi, Facile synthesis of highly thermally stable TiO_2 photocatalysts, New J. Chem. 41 (2017) 5021–5027. doi:10.1039/C7NJ00747G.

[97] Q. Pan, C.-C. Chung, N. He, J.L. Jones, W. Gao, Accelerated Thermal Decomposition of Graphene Oxide Films in Air via in Situ X-ray Diffraction Analysis, J. Phys. Chem. C. 120 (2016) 14984–14990. doi:10.1021/acs.jpcc.6b05031.

[98] L.M. Pastrana-Martínez, S. Morales-Torres, V. Likodimos, P. Falaras, J.L. Figueiredo, J.L. Faria, A.M.T. Silva, Role of oxygen functionalities on the synthesis of photocatalytically active graphene–TiO_2 composites, Appl. Catal. B Environ. 158–159 (2014) 329–340. doi:10.1016/j.apcatb.2014.04.024.

[99] M. Sohail, M. Saleem, S. Ullah, N. Saeed, A. Afridi, M. Khan, M. Arif, Modified and improved Hummer's synthesis of graphene oxide for capacitors applications, Mod. Electron. Mater. 3 (2017) 110–116. doi:10.1016/j.moem.2017.07.002.

[100] D.M. Tobaldi, C. Piccirillo, R.C. Pullar, A.F. Gualtieri, M.P. Seabra, P.M.L. Castro, J.A. Labrincha, Silver-Modified Nano-titania as an Antibacterial Agent and Photocatalyst, J. Phys. Chem. C. 118 (2014) 4751–4766. doi:10.1021/jp411997k.

[101] A. Giampiccolo, D. Maria, S. Gianluca, B. James, M. Paula, M.P. Ansell, G. Neri, R.J. Ball, Applied Catalysis B : Environmental Sol gel graphene / TiO_2 nanoparticles for the photocatalytic-assisted sensing and abatement of NO_2, Appl. Catal. B Environ. 243 (2019) 183–194. doi:10.1016/j.apcatb.2018.10.032.

[102] N. Serpone, R. Khairutdinovt, Size Effects on the Photophysical Properties of

Colloidal Anatase TiO_2 Particles: Size Quantization or Direct Transitions in This Indirect Semiconductor?, J. Phys. Chem. 02 (1995) 16646–16654. doi:10.1021/j100045a026.

[103] K. Madhusudan Reddy, S. V Manorama, A. Ramachandra Reddy, Bandgap studies on anatase titanium dioxide nanoparticles, Mater. Chem. Phys. 78 (2003) 239–245. doi:10.1016/S0254-0584(02)00343-7.

[104] X. Hu, T. Mohamood, W. Ma, C. Chen, J. Zhao, Oxidative Decomposition of Rhodamine B Dye in the Presence of VO_2^+ and/or Pt(IV) under Visible Light Irradiation: N-Deethylation , Chromophore Cleavage, and Mineralization, J. Phys. Chem. B. 110 (2006) 26012–26018. doi:10.1021/jp063588q.

[105] R. Leary, A. Westwood, Carbonaceous nanomaterials for the enhancement of TiO_2 photocatalysis, Carbon N. Y. 49 (2011) 741–772. doi:10.1016/j.carbon.2010.10.010.

[106] M.J. Sampaio, C.G. Silva, A.M.T. Silva, L.M. Pastrana-Martínez, C. Han, S. Morales-Torres, J.L. Figueiredo, D.D. Dionysiou, J.L. Faria, Carbon-based TiO_2 materials for the degradation of Microcystin-LA, Appl. Catal. B Environ. 170–171 (2015) 74–82. doi:10.1016/j.apcatb.2015.01.013.

[107] Q. Yi, J. Ji, B. Shen, C. Dong, J. Liu, J. Zhang, M. Xing, Singlet Oxygen Triggered by Superoxide Radicals in a Molybdenum Cocatalytic Fenton Reaction with Enhanced REDOX Activity in the Environment, Environ. Sci. Technol. 53 (2019) 9725–9733. doi:10.1021/acs.est.9b01676.

[108] D.M. Tobaldi, L. Lajaunie, N. Rozman, A.P.F. Caetano, M.P. Seabra, A. Sever Škapin, R. Arenal, J.A. Labrincha, Impact of the absolute rutile fraction on TiO_2 visible-light absorption and visible-light-promoted photocatalytic activity, J. Photochem. Photobiol. A Chem. 382 (2019) 111940.

doi:10.1016/j.jphotochem.2019.111940.

[109] A. Ajmal, I. Majeed, R.N. Malik, H. Idriss, M.A. Nadeem, Principles and mechanisms of photocatalytic dye degradation on TiO_2 based photocatalysts: a comparative overview, RSC Adv. 4 (2014) 37003–37026. doi:10.1039/C4RA06658H.

Highlights

- TiO_2 and carbon-modified TiO_2 photocatalysts are prepared with different properties;
- The materials behave as photocatalysts on the degradation of organics from air and water;
- Carbon-modified TiO_2 led to enhanced degradation of both RhB and benzene under Vis light;
- CNT- and GO-modified materials, treated at 300 °C, outperformed Degussa P25.
- The photocatalyst was successfully reused, up to 6 times, on the degradation of benzene.

Graphical abstract